Overview of the FTU results – 2017

✓ Runaway Electrons
- Runaway Electrons generation and suppression
- Runaway beam control
- Runaway generation during EC assisted plasma start-up

✓ Transport studies
- Neon impurity injection
- Thermo-diffusion in particle transport
- Ion drift effects on MARFE

✓ MHD activity in the high-density regime
- Density limit scaling laws
- Tearing mode onset
- MHD limit cycles

✓ Plasma Facing Components
- Liquid Lithium Limiter
- Tungsten enrichment of surface layer
- Dust studies

✓ Diagnostics
- Fast infrared camera
- Collective Thomson Scattering
- Triple-GEM detector
- Cherenkov probe
- Runaway Electrons Imaging and Spectroscopy

Runaway Electrons generation

- Experiments of RE onset and suppression in ohmic pulses have confirmed that the measured critical electric field for RE generation (E_{trh}) is 2÷5 times larger than predicted by the relativistic collisional theory (E_R) and consistent with the new threshold (E_R^{rad}) calculated including synchrotron radiation losses.
- The RE onset and suppression experiments provide, respectively, upper and lower bounds for the critical field.

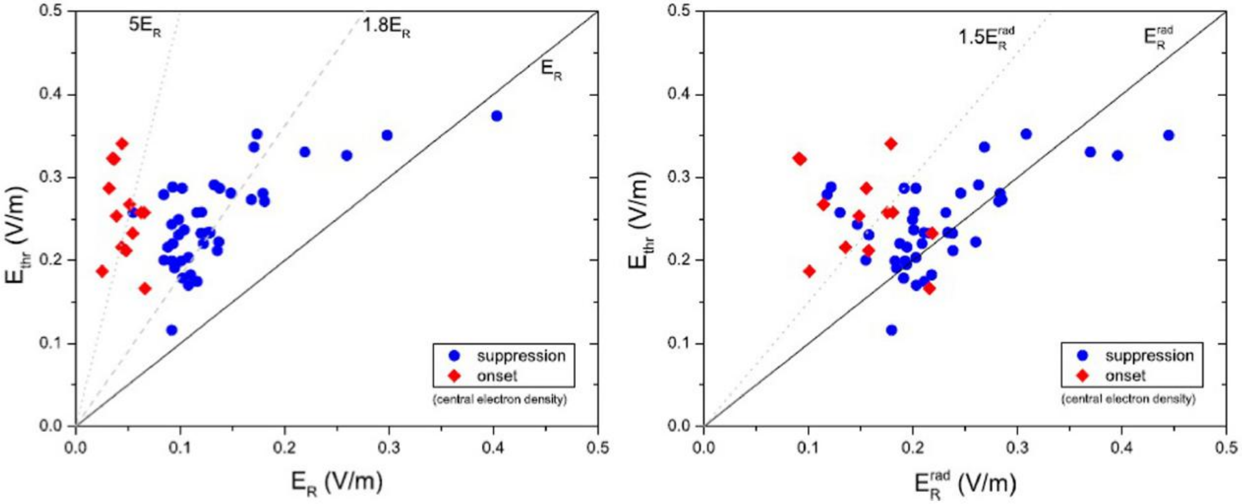

$$E_R = \frac{n_e e^3 \ln \Lambda}{4\pi \epsilon_0^2 m_e c^2}$$

$$\frac{E_R^{\mathrm{rad}}}{E_R} \cong 1 + C_{(Z_{\mathrm{eff}})} \left(\frac{2\epsilon_0 B^2}{3 m_e n_e \ln \Lambda} \right)^{0.45}$$

Figure 1. *Comparison of measured E_{thr} with relativistic collisional (left) and collisional+synchrotron radiation (right) theory predictions. The local central density is used to calculate E_R since RE are initially generated in the core of the plasma.*

Esposito B. PPCF **59** (2017)

Runaway Electrons beam control

- ❑ A new RE control algorithm for real-time control of post disruption RE beam has been tested, in order to minimize the interaction with plasma facing components while RE current is ramped-down by induction. Fission chambers signals show reduced plasma facing components interaction with the new controller active.

- ❑ The study has revealed that the decay rate during RE beam current ramp-down is a key parameter for runaway current suppression.

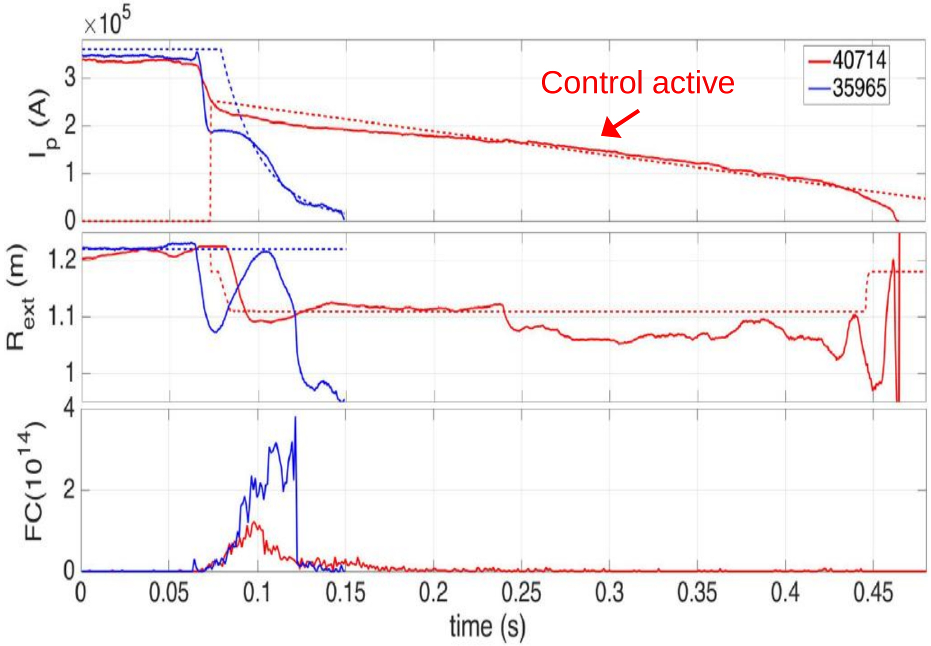

Figure 2. *Experimental tests of RE control algorithm. The RE beam current, the RE beam external radius and the signal from the 235 U fission chamber are reported in the different panels.*

Carnevale D. IAEA EX/P8-22 (2016)

EC assisted plasma start-up

- Experiments of EC assisted plasma start-up have shown the generation of RE even at moderate EC power injection, in condition of toroidal electric field E_{Loop} well below the Dreicer field threshold E_D for primary generation, evidencing that EC wave acts as a seeding for fast electrons, that are further accelerated by the toroidal electric field.
- A dependency of the RE generation on the pre-filling pressure has been observed. There are results that indicate the absence of RE in case of injection of waves in XM2 polarization.

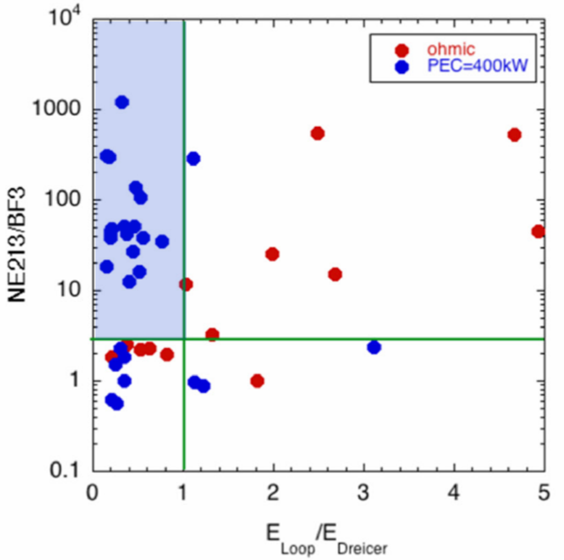

Figure 3. *RE presence as a function of toroidal electric field normalized to the Dreicer threshold for pure ohmic and EC assisted pulses.*

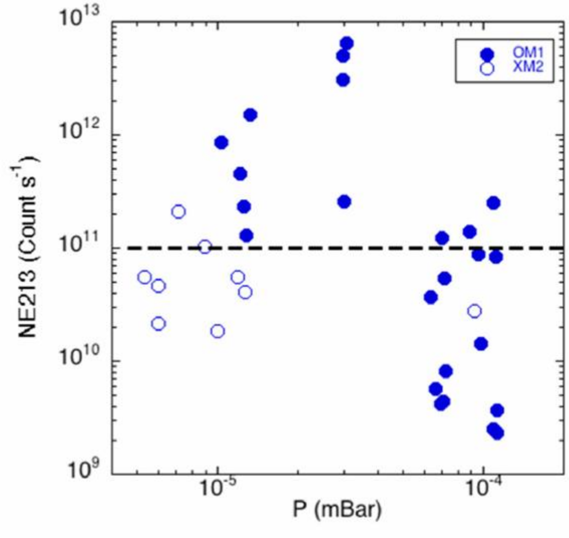

Figure 4. *Signal from gamma ray detector as a function of pre-filling pressure. Below 10^{11} counts no RE presence can be assumed.*

Granucci G. EPS P5.020 (2016)

Neon impurity injection

❑ A linear micro-stability analysis of a Neon doped pulse has been carried out with the gyro-kinetic code GKW to investigate the mechanisms leading to the observed density peaking.

❑ The simulation of the Neon doped pulse, performed with a density impurity profile reconstructed by means of an impurity transport code, has been compared with the simulation of a similar un-doped pulse.

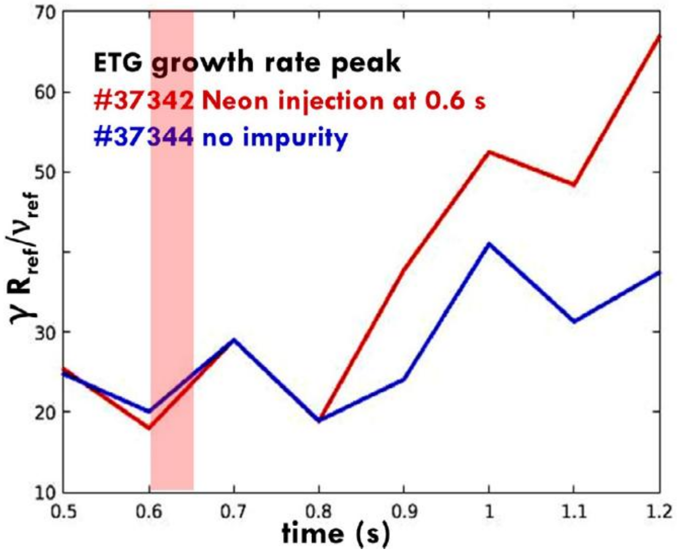

Figure 5. *Time traces of the ETG peaks at r/a = 0.5. The red vertical box highlights the Neon injection period for the pulse # 37342. The impurity employs 150 ms to reach and to penetrate plasma.*

Mazzotta C. EPS P5.019 (2016)

❑ The fluxes analysis shows that Electron Temperature Gradient (ETG) modes drive the inward flux for all the species and everywhere, so that the sharp peaking of the density profile is mainly due to the inward pinch brought about by ETG modes.

Thermo-diffusion in particle transport

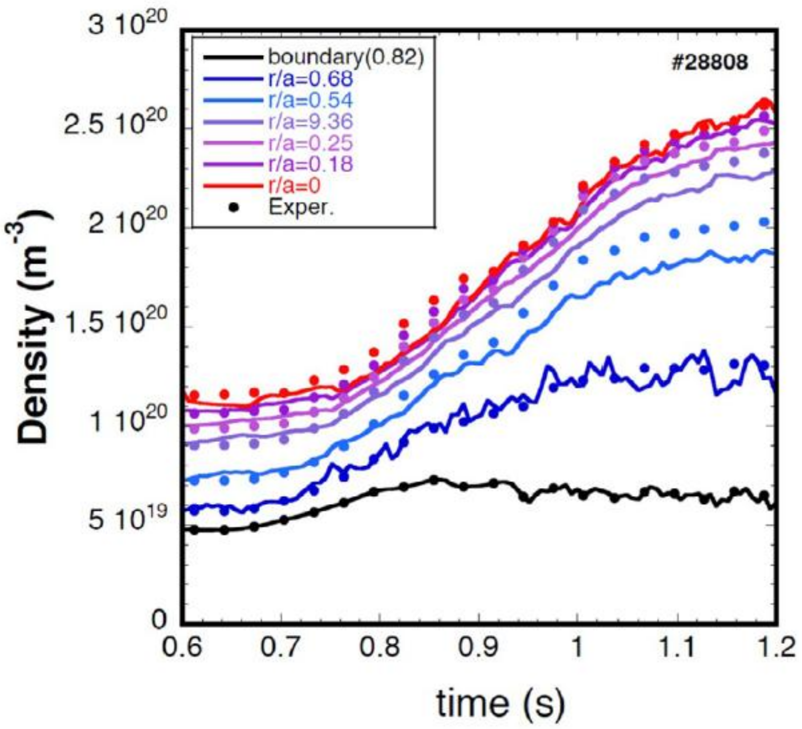

Figure 6. *Simulation of density evolution at different normalized plasma radius. Calculated density (lines) are well in agreement with experimental data (dots).*

Tudisco O. IAEA EX/P8-24 (2016)

- A set of pulses has been performed in the high-density regime, evidencing a sensible density peaking, subsequent the formation of a strong MARFE thermal instability.
- A neutral diffusion code has been used to estimate the contribution of neutral to particles balance, showing that the source term remains negligible across most of the plasma section.
- The density profile evolution has been well reproduced using a particle pinch term with dependence on temperature gradients:

$$\Gamma_p = -D_{\mathrm{T}} \frac{n_e}{T_e} \frac{\partial T_e}{\partial r}$$

Ion drift effects on MARFE

- A study of the ion drift effects (∇B and curvature drifts) on the MARFE instability has been performed, including pulses with reversed toroidal magnetic field direction and pushing the plasma column towards the High Field Side and Low Field Side, respectively.

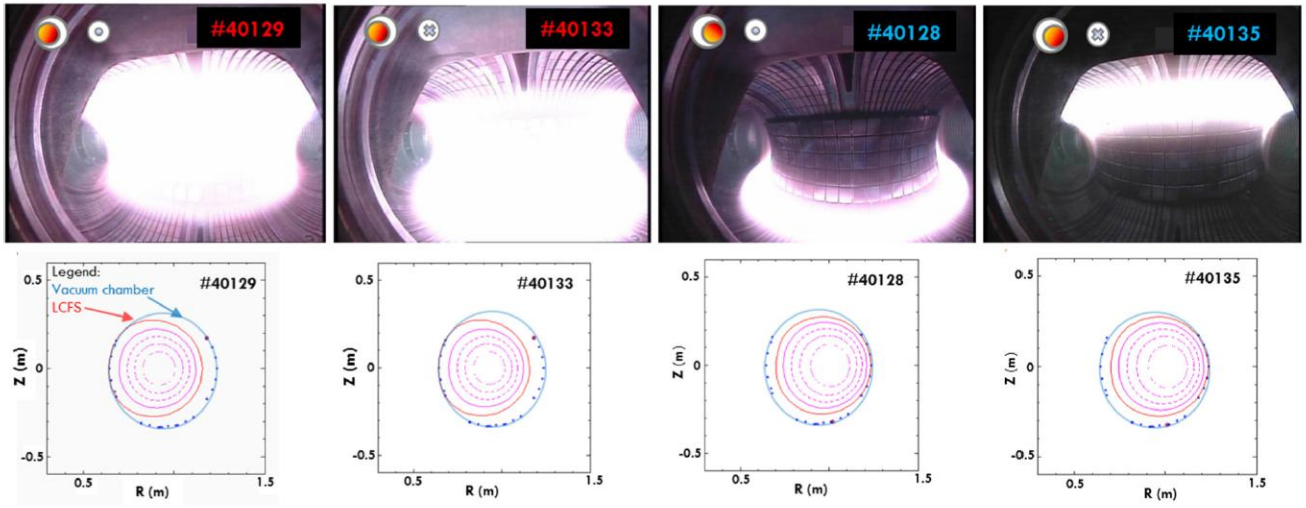

Figure 7. Visible camera images and flux maps for the four different configurations performed.

- For the two configurations with the plasma pushed towards the LFS, the MARFE is detached from the internal toroidal limiter, and it is positioned in the upper or lower mid plane, in agreement with the direction of the ion drift velocity.

$$\vec{v}_D = \frac{(v_\perp^2/2 + v_\parallel^2)}{\Omega R}\hat{R}\times\hat{B}$$

Mazzotta C. PSI P4.42 (2016)

Density limit scaling laws

- Dedicated density limit experiments were performed, confirming the edge nature of the density limit, as a Greenwald-like scaling was obtained for the maximum achievable line-averaged density along a peripheral chord with normalized radius r/a=0.8.
- The scaling of the maximum achievable line-averaged density along a central chord (r/a=0) with the toroidal magnetic field only was successfully interpreted as due to interplay between the Greenwald edge limit and the specific density profile behavior when approaching the density limit, with the density peaking linearly depending on the edge safety factor.

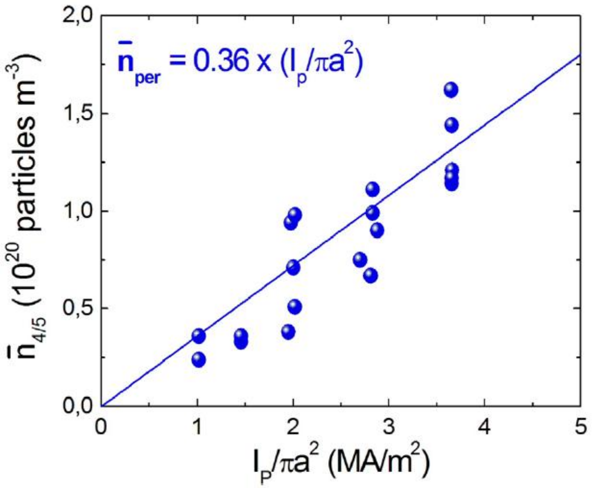

Figure 8. *Line-averaged density for a peripheral chord (r/a = 4/5) at the disruption versus the plasma current density.*

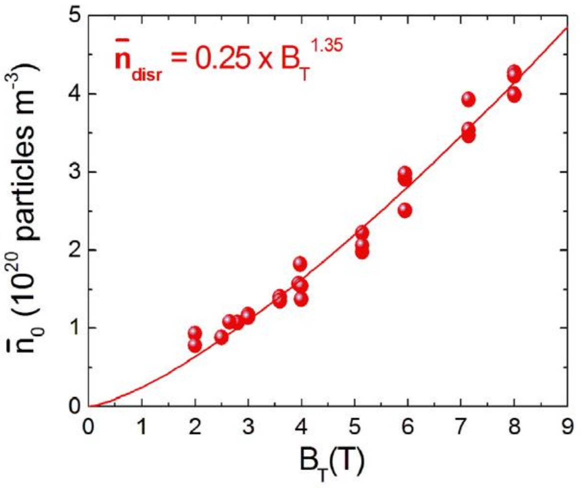

Figure 9. *Line-averaged density for a central chord (r/a = 0) at the density limit disruption versus the toroidal magnetic field.*

Pucella G. PPCF **59** (2017)

Tearing mode onset

- Density limit disruptions are usually ascribed to a thermal instability occurring when the radiation loss near the edge region overcomes the heat flux emerging from the core.

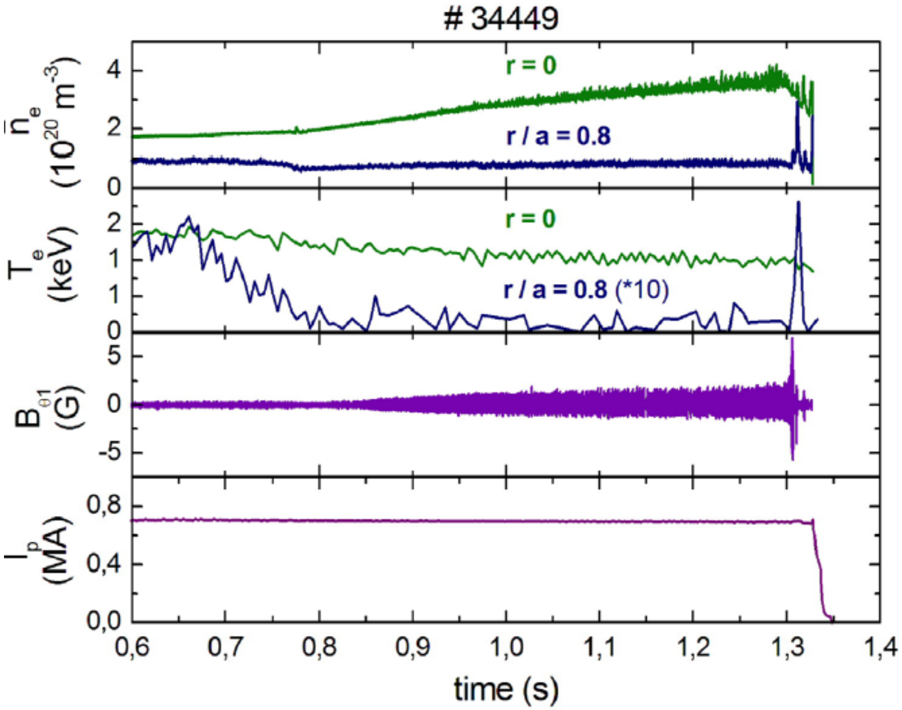

Figure 10. *Time traces of some relevant quantities for MHD activity on FTU: central and peripheral line-averaged density, poloidal magnetic perturbation, central and peripheral electron temperature, plasma current.*

Pucella G. EPS P5.139 (2013)

- The analysis of the linear stability of a 2/1 tearing mode in high density plasmas, performed by means of a Δ' code in cylindrical geometry and by means of the complete linear resistive MHD code MARS, has highlighted a destabilization with increasing peaking of the current profile during the density ramp-up, in agreement with the experimental observations.

MHD limit cycles

- The MHD activity in proximity of the density limit shows a 2/1 tearing mode growing up to high amplitude, with a final phase characterized by amplitude and frequency oscillations, giving rise to limit cycles on the amplitude/frequency plane.

- Amplitude and frequency modulations could be caused by island self-healing phenomena, with a recursive island fragmentation, as supported by the observation of spatial harmonics that grow and strongly distort the island shape before each amplitude drop.

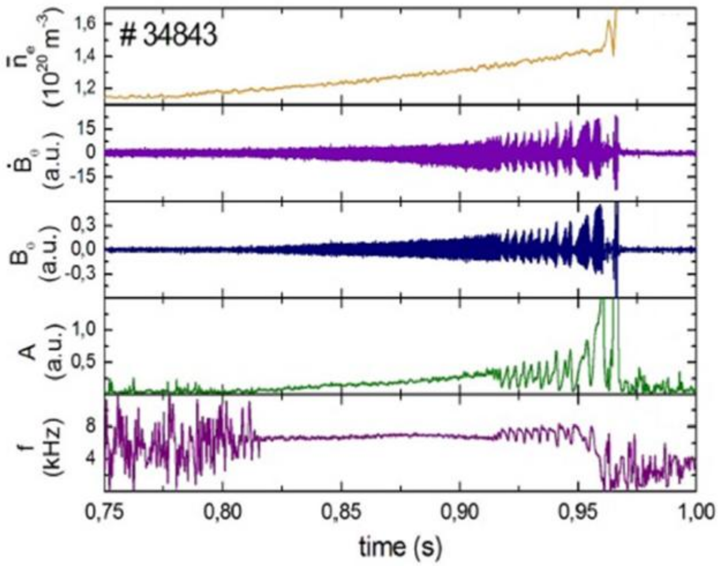

Figure 11. *Time traces of some relevant quantities for the MHD activity.*

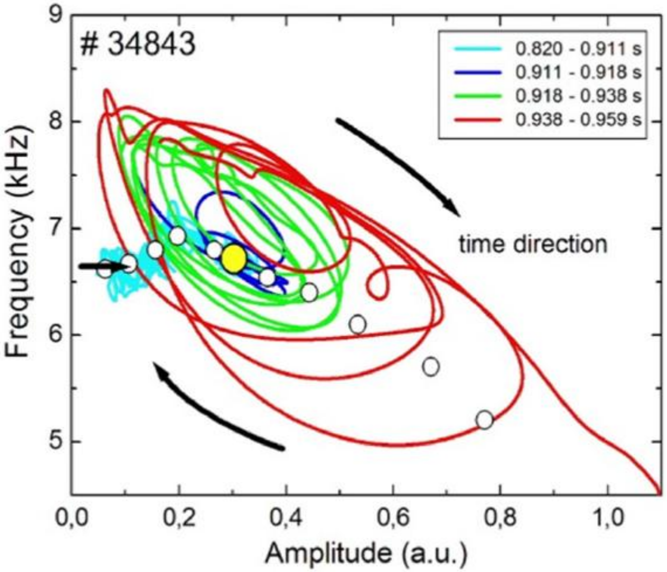

Figure 12. *Tearing mode time evolution on the plane Amplitude/Frequency.*

Pucella G. EPS P4.112 (2015)

Liquid Lithium Limiter

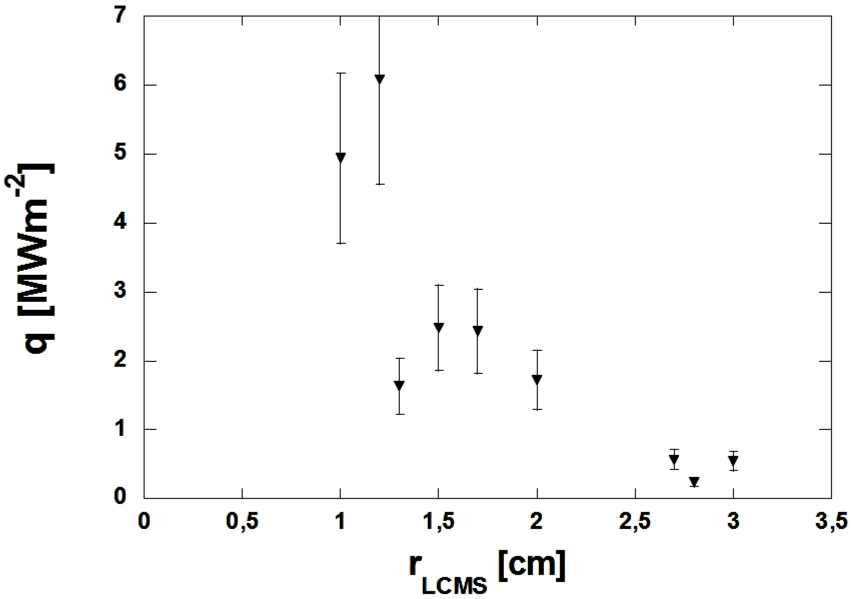

Figure 13. *Heat loads on LLL in stationary conditions for pulses with different distance from the last closed magnetic surface.*

Mazzitelli G. IAEA EX/P8-21 (2016)

- Extremely encouraging test performed on the standard Liquid Lithium Limiter (LLL), showing heat loads up to 5 MW/m^2 with no damage.

- A Cooled Lithium Limiter (CLL) with reactor relevant thermal load capability up to 10 MW/m^2 has been realized and implemented on FTU for the next experimental campaigns.

- In preparation of the next CLL experiments, the pulse duration for lower plasma currents (0.25-0.35 MA) has been extended up to 4.5 s, to test the CLL in stationary high heat flux conditions.

- To maximize and control heat load on limiter, elongated configurations (k ~ 1.2) have been obtained for 3.5 s, with the X-point just outside the plasma chamber.

Tungsten enrichment of surface layer

- A P92 steel sample with a low W concentration (~1%) was exposed in the SOL during steady state pulses, with the purpose of checking the effectiveness of preferential sputtering in the W enrichment of the very surface layer of first wall material, like EUROFER steel.

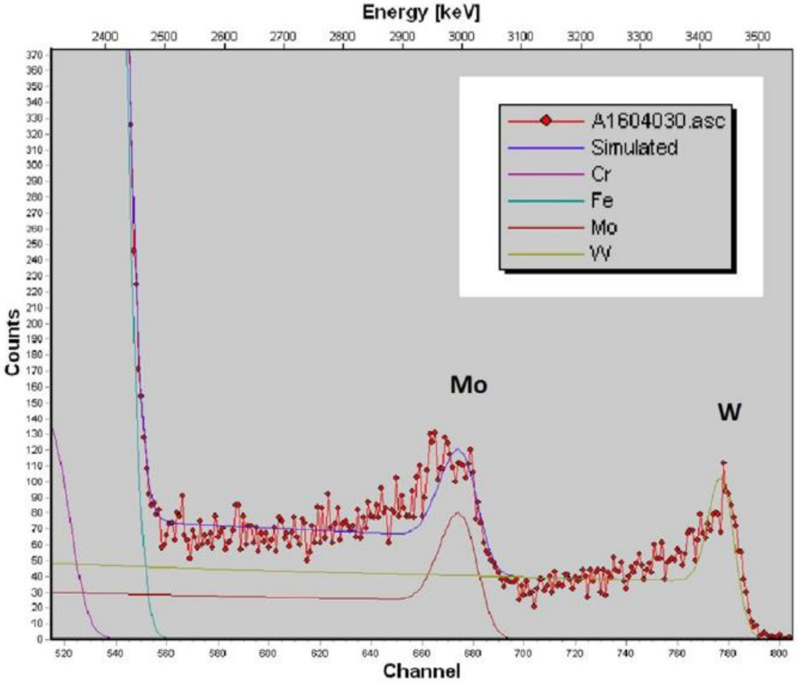

Figure 14. *RBS spectrum of P92 sample showing the W and Mo surface enrichment.*

- Rutherford Backscattering Spectrometry (RBS) analysis of the exposed sample shows, with respect to a non exposed one, a surface enrichment of both W and Mo, the latter probably coming also from the TZM toroidal limiter and/or the Mo outer poloidal limiter.

Maddaluno G.

Dust studies

- Dust from FTU has been collected and analyzed and it was found that the metallic population exhibits a high fraction (up to 70 wt%) of magnetic grains, that could be lifted-up during the ramping-up phase of the toroidal magnetic field due to ∇B force and interfere with the start up phase of plasma pulse.

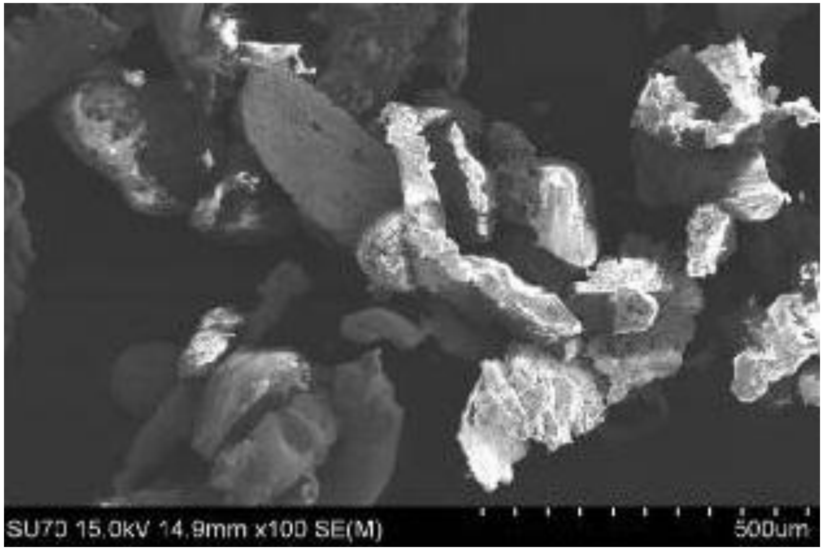

Figure 15. *SEM images of ferromagnetic particles collected by a permanent magnet.*

- The origin of ferromagnetic dust is related to the molten drops ejected by austenitic stainless steel (non-magnetic) PF Components (such as first walls, diagnostics, antennas, etc.), where the crystalline phase of iron changes from non-magnetic to magnetic phase.

De Angeli M. NF **55** (2015)

Fast infrared camera

- ☐ The thermo-graphic analysis of the inboard toroidal limiter has been carried out, transferring the image of one sector to an infrared camera. Several disruptions have been monitored, providing the pattern of limiter heating by disruption heat loads.

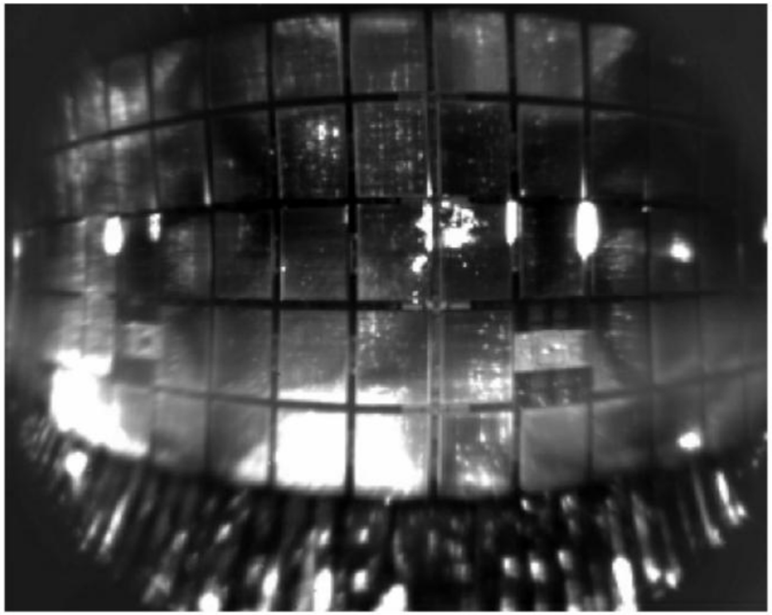

Figure 16. *Post-disruption infrared image of a toroidal limiter sector.*

- ☐ Complementary to the measurement of thermal load is the detection of eroded or mobilized dust. Its survival in the vacuum chamber for long time after the disruption confirms the indirect detection carried out in the past with Thomson scattering diagnostic.

Maddaluno G.

Collective Thomson Scattering

- Investigation on possible excitation of Parametric Decay Instabilities by EC beams in presence of magnetic islands using the CTS diagnostic, launching a gyrotron probe beam (140 GHz, 400 kW) and receiving the CTS beam in symmetric and asymmetric configurations with respect to the equatorial plane, with or without the EC resonance in the plasma.

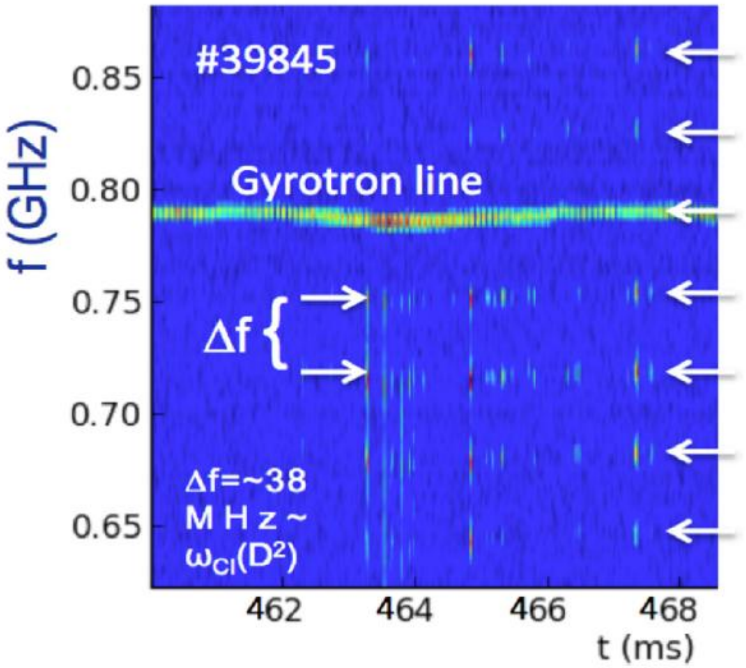

Figure 17. Asynchronous sequence of bursts emitted at frequency multiple of the deuteron ion cyclotron frequency above and below the gyrotron line, occurring in connection with an MHD activity leading to plasma disruption.

- The CTS diagnostic was renewed with the acquisition of a fast digitizer, which allowed the observation of several spectral features with very high time and frequency resolution.

Bruschi A. IAEA EX/P8-23 (2016)

Triple-GEM detector

- A triple-GEM (gas electron multiplier) detector has been tested on FTU for soft-X rays diagnostic. The detector is equipped with a read-out anode having 128 pads distributed along a vertical line. Each pad has an area of 500×500 µm^2 (with a pitch of 700 µm) and a field of view of 1.4×1.4 mm^2 on the plasma, according to the realized geometrical configuration.

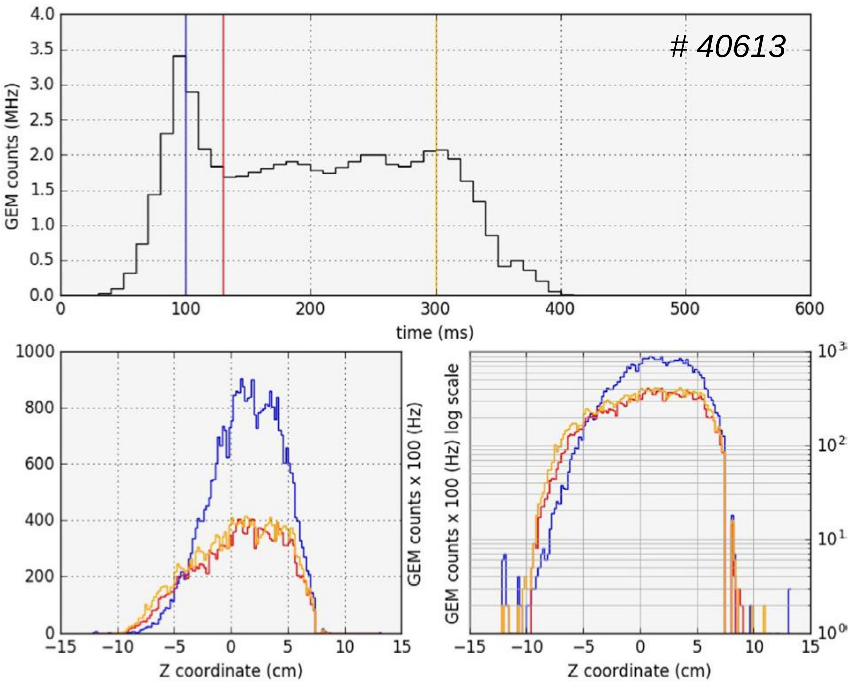

Figure 18. *(Top) Temporal trace as measured from the GEM detector, obtained summing on all the pad counts. (Bottom) Plasma profiles measured by the GEM detector at different times.*

- Two GEM cameras (with vertical and horizontal orientation) will be installed in the future on FTU, in order to realize a more performing tomography system respect to the conventional diode system.

Pacella D. EPS P5.118 (2013)

Cherenkov probe

- In the presence of Beta-induced Alfvén Eigenmodes (BAE) associated to high amplitude magnetic islands, the Cherenkov probe has detected bursty expulsions of RE modulated by the island rotation frequency, indicating that RE losses promptly respond to island amplitude fluctuations (first detection of BAE using a non-magnetic plasma diagnostics).

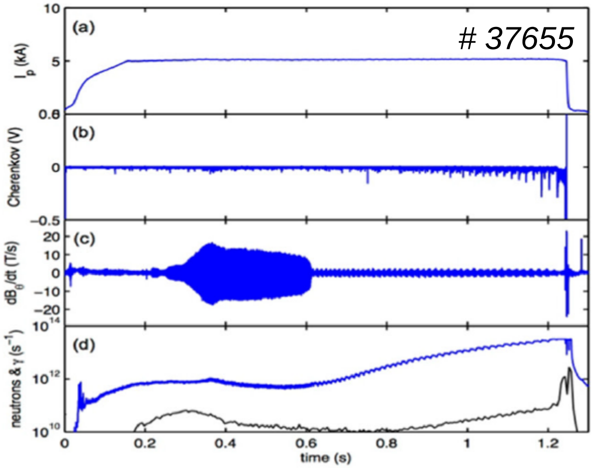

Figure 19. Scenario involving island quasi locking and BAE: plasma current, Cherenkov signal, Mirnov coils, NE213 and BF3 (black line) signals.

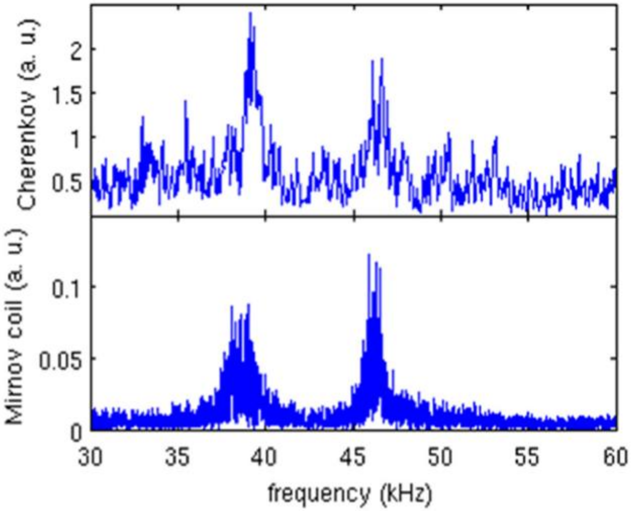

Figure 20. Power spectral density in the high frequency range of (top) Mirnov and (bottom) Cherenkov signals.

- A system upgrade that will enable energy and spatially resolved analysis of RE losses is planned, to evaluate the potential of this diagnostics for implementation in fusion reactors.

Causa F. NF **55** (2015)

RE Imaging and Spectrometry

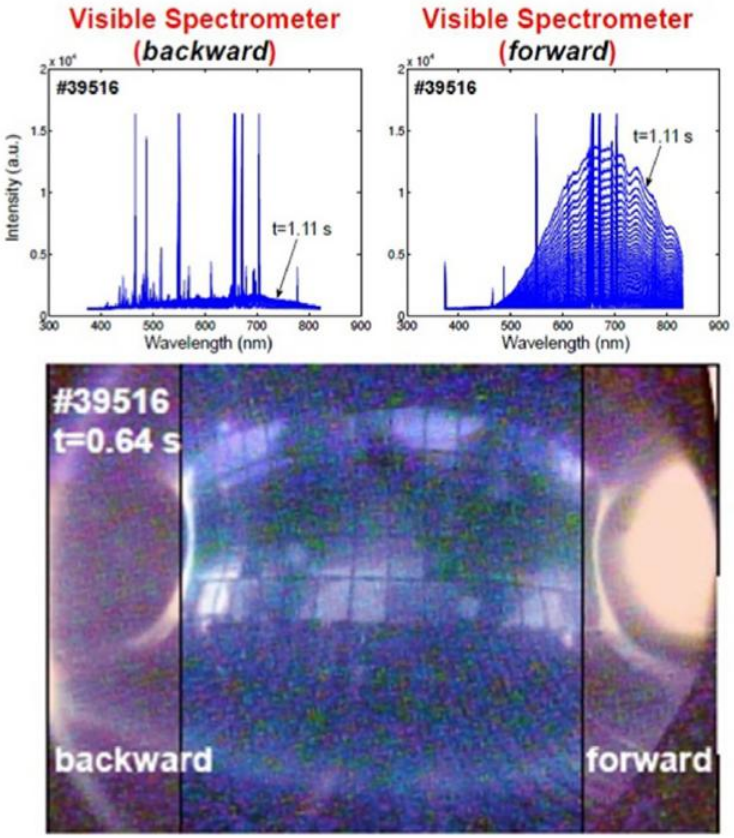

__Figure 21.__ (Top) RE visible camera image for a runaway pulse; the visible spectra show also the impurity spectral lines. (Right) Infrared spectrum of the forward radiation; an attenuation gap due to the transmission fibers is present.

- A new diagnostic has been developed specifically to analyze the synchrotron radiation from in-flight RE, allowing to provide simultaneously the image and the visible/infrared spectrum of the forward and backward radiation.
- Information on the RE energy distribution function in the various phases of a plasma pulses, and particularly during runaway plateaus following disruption events, can be obtained.

Esposito B. EPS I4.116 (2016)